11 May 2021

Tuning Polymorphs and Morphology of Microbially Induced Calcium Carbonate: Controlling Factors and Underlying Mechanisms

Maryam Khanjani

David J. Westenberg
Missouri University of Science and Technology, djwesten@mst.edu

Aditya Kumar
Missouri University of Science and Technology, kumarad@mst.edu

Hongyan Ma
Missouri University of Science and Technology, mahon@mst.edu

Recommended Citation

M. Khanjani et al., "Tuning Polymorphs and Morphology of Microbially Induced Calcium Carbonate: Controlling Factors and Underlying Mechanisms," *ACS Omega*, vol. 6, no. 18, pp. 11988-12003, American Chemical Society (ACS), May 2021.
The definitive version is available at https://doi.org/10.1021/acsomega.1c00559

ACS OMEGA

http://pubs.acs.org/journal/acsodf

Article

Tuning Polymorphs and Morphology of Microbially Induced Calcium Carbonate: Controlling Factors and Underlying Mechanisms

Maryam Khanjani, David J. Westenberg, Aditya Kumar, and Hongyan Ma*

Cite This: *ACS Omega* 2021, 6, 11988−12003

Read Online

ACCESS | Metrics & More | Article Recommendations

ABSTRACT: Microbially precipitated calcium carbonate ($CaCO_3$) has drawn broad attention due to its potential applications in various areas, for example, biocementation, medicine, and soil reinforcement. *Sporosarcina pasteurii* (*S. pasteurii*), formerly known as *Bacillus pasteurii*, has been investigated for $CaCO_3$ biomineralization due to its high ureolytic activity. A high degree of supersaturation with respect to the presence of bacterial cell wall, extracellular polymeric substances, and organic byproducts of bacterial activity plays an important role in the formation and stabilization of $CaCO_3$ polymorphs. Although microbially induced $CaCO_3$ and its polymorphs have been investigated broadly, the mechanisms of polymorph selection and morphological evolution are not well understood. This study employs ex situ approaches to address the complication of biomineralization in the presence of living organisms and to elucidate how solution chemistry, bacterial activity, and precipitation kinetics alter the polymorphism and morphology of $CaCO_3$ induced by *S. pasteurii*. The results indicate that in the presence of enough calcium ions and urea (as a carbonate source), the bacterial activity favors the formation and stabilization of vaterite. The morphological observations also provide valuable information on the particles' microstructure. The morphology of calcite evolves from single crystal to polycrystalline structures, and the morphology of vaterite evolved from spherical to oval-shaped structures on increasing the organic material concentration. Specific functional groups also exert morphological control on $CaCO_3$ polymorphs. However, the sensitivity of the calcite polymorph to the composition and orientation of these functional groups is higher compared to that of the vaterite polymorph. These findings offer important insights that can be used to constrain a set of experimental conditions for synthesizing a certain polymorph ratio for vaterite/calcite or a particular morphology of each polymorph and shed light on the crystallization and phase transformation mechanisms in such complicated bioenvironments.

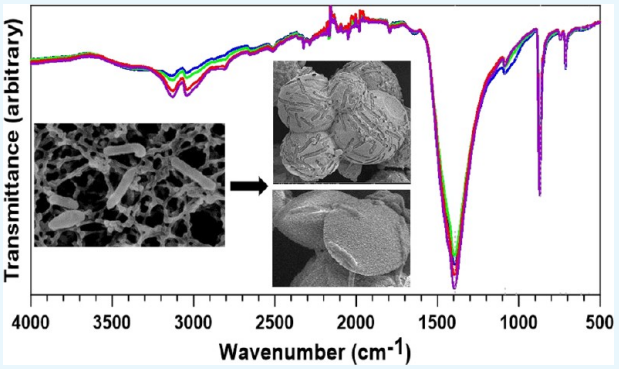

1. INTRODUCTION

Morphological manipulation of biominerals during biomineralization holds great promise in biological, biochemical, and biomedical uses as well as industrial applications of the minerals obtained. Meanwhile, biomineralized calcium carbonate ($CaCO_3$) has drawn broad attention due to its potential applications in various areas, such as biocementation,[1] medicine,[2] and soil reinforcement.[3] This is because $CaCO_3$ is a polymorphic material that exhibits three anhydrous polymorphs—calcite, aragonite, and vaterite,[4,5] which makes it an attractive test material for manipulating production of these polymorphs. The ability of $CaCO_3$ to produce a wide range of morphologies[6−10] also necessitates studying the effects of different additives on the morphological evolution of this biomineral.

Organic compounds have been shown to affect the chemical and physical properties of calcium carbonate precipitates.[11−14] Urea decomposition has also been found to induce $CaCO_3$ precipitation in aqueous solution when calcium ions are present.[15,16] Therefore, some studies have focused on the effects of enzymes such as urea amidohydrolase (urease) on inducing $CaCO_3$ precipitation.[17] The ability of urease to decompose urea makes it a great choice for the preparation of metal carbonates.[18] Furthermore, hydrolysis of urea can be easily controlled and has the potential to produce high amounts of CO_3^{2-} within a short period of time.[19] Hence, there has been significant interest in ureolytic microorganisms such as *Bacillus sphaericus*,[20] *Bacillus megaterium*,[21,22] and *Lysinibacillus sphaericus*[23] that can hydrolyze urea to induce $CaCO_3$ precipitation.[24−27] Also, it has been suggested that the

Received: January 30, 2021
Accepted: April 21, 2021
Published: April 29, 2021

bacterial cell wall can provide nucleation sites as it carries negatively charged functional groups.[24,25,28−33] These negative charges can attract Ca^{2+} on the cell surface, which serve as nucleation sites for the reaction of Ca^{2+} and CO_3^{2-} to proceed.[24,32,34] A definitive proof of the cellular level contribution of the bacterium in $CaCO_3$ precipitation and involvement of the bacterial cell surface on the nucleation process is, however, limited.

Sporosarcina pasteurii (*S. pasteurii*) (formerly known as *Bacillus pasteurii*), a nonpathogenic, endospore-forming, ureolytic soil bacterium, has been extensively investigated for its ability to precipitate $CaCO_3$.[20,35−40] However, the underlying mechanism that controls the growth and crystallization process remains unclear and controversial. The dynamics of nucleation, including the formation of the early stage nuclei, growth and crystallization process, and the transformation of potential intermediate phases, typically occur at nanometer length scales. This limits the utility of in situ identification methods. In other words, in the absence of sufficient techniques to study in situ mineralization mechanisms, indirect approaches have to be employed to provide further insights into the biomineralization process.

So far, various nucleation and growth theories have been employed to explain the $CaCO_3$ precipitation process, and they can be classified into two broad types—classical and nonclassical theories. The classical nucleation and growth theory follows Gibbs equilibrium principles[41] suggesting that nucleation in electrolyte solutions takes place via unstable density fluctuations due to attachment and detachment of monomers (e.g., atoms, ions, and molecules). After a sufficient time, a nucleus randomly forms, and if it exceeds the critical size, further growth will be energetically favorable and proceeds via monomer-by-monomer attachment to the existing nuclei in the presence of sufficient material sources.[41]

In an effort to explain the phase transformation in a polymorphic material, Ostwald's law of stages was proposed suggesting that the phase transformation proceeds in a sequential event from an unstable state to the metastable state and eventually to the most stable state and such sequential events are an inevitable consequence of the thermodynamic tendency of the system to minimize its free energy.[42] Later, the solvent-mediated transformation theory was proposed to explain the mechanism of phase transformation in a polymorphic system. According to this theory, transformation of a metastable phase, which is in contact with a solvent, to the stable phase proceeds via dissolution of the metastable phase and independent nucleation and growth of the stable phase from solution.[43]

Recently, in an attempt to explain the very early stage of $CaCO_3$ nucleation and crystallization, a nonclassical nucleation theory has been proposed.[44] According to this theory, stable multi-ion species named "prenucleation clusters" form prior to the formation of the crystalline phases. These clusters later aggregate to form amorphous calcium carbonate (ACC) precursors including proto-vateritic ACC[45] and proto-calcitic ACC[45,46] that each subsequently transform to the respective crystalline phases via a distinct crystallization event.[44]

In the case of electrolyte solutions, knowledge is still lacking as to whether the classical nucleation theory[41] is a suitable framework to describe the nucleation and crystallization process or nonclassical elements such as prenucleation clusters[44] play the key roles. Furthermore, it is still unclear whether a final stable phase can nucleate directly from solution or it forms through a multistep, multiphase evolution.[47] In the case of multistep nucleation pathways, whether transformation from one phase to another occurs through dissolution of the metastable phase and reprecipitation of the stable phase is also unclear.[48,49] That is to say, theories are still inefficient in predicting the formation of polymorphs in different stages.

In this study, we employ ex situ approaches to investigate the sensitivity of $CaCO_3$ precipitation in the presence of bacterial cells to various biological, chemical, and physical parameters. Instead of modeling the nucleation, crystallization, and phase transition of $CaCO_3$, we aim to establish a pathway to predict and control precipitation outcomes by identifying the factors that control the $CaCO_3$ polymorph selection (e.g., a specific product consisting of predetermined proportions of different polymorphs). The morphological investigations of the precipitates also allow us to address the $CaCO_3$ growth and crystallization mechanisms qualitatively. Our results can be used to constrain a set of experimental conditions for synthesizing a certain polymorph ratio for vaterite/calcite or a particular morphology of each polymorph.

2. RESULTS AND DISCUSSION

In crystallization processes with more than one phase involved, the control of kinetic factors is crucial in order to obtain the desired phase combinations. Metastable phases can easily degrade or undergo phase transformation.[43,50] Therefore, to produce and preserve a metastable phase, a large driving force is often needed. In the case of $CaCO_3$ precipitation, the appearance and stabilization of metastable phases during biomineralization are associated with the environmental conditions at the time of precipitation.[51] Organic materials have been shown to contribute to the $CaCO_3$ nucleation and crystallization process by acting as templates that direct the interaction and orientation of the individual crystallites,[6,68−70] and subsequently, stabilizing the metastable phases. Therefore, understanding the underlying mechanisms that control the growth and crystallization process during biomineralization holds considerable importance and allows researchers to manipulate the process in order to produce and stabilize desirable polymorphic minerals.

In this research, the experiments were performed in two sets: first, to examine the effect of Ca^{2+} and urea concentrations on the polymorph selection and morphological evolution of the bacterially precipitated $CaCO_3$; second, to study the $CaCO_3$ nucleation and crystallization process at the microscale level by monitoring the kinetics of a biomineralization solution over a time period of 30 days. All experiments were carried out at an initial pH of 9.00 and 30 °C under the conditions listed in Table 1. Phase identification for all samples was performed by powder X-ray diffraction (XRD), and the incorporation of organic compounds in the structure of $CaCO_3$ polymorphs was examined by Fourier transform infrared (FTIR) and energy-dispersive X-ray spectroscopy (EDS) techniques.

Figure 1a,b shows the FTIR spectra for the effects of Ca^{2+} and urea concentrations and time-dependent kinetics of the biomineralization solution experimental sets, respectively. The vibrational bands at 1086, 876, and 744 cm^{-1} correspond to symmetric carbonate stretching (ν_1 mode), carbonate out-of-plane bending (ν_2 mode), and in-plane bending (ν_4 mode) vibrations, respectively, which are characteristic vibrational bands of vaterite,[55−60] and the main carbonate band of vaterite (asymmetric stretching, v_3 mode) was detected at 1400 cm^{-1}.[61] Vibrational bands at 876 and 713 cm^{-1} correspond

https://doi.org/10.1021/acsomega.1c00559
ACS Omega 2021, 6, 11988−12003

Table 1. Experimental Conditions and Calcium Carbonate Precipitate Characteristics[a]

sample	conc. of Ca^{2+} (M)	conc. of urea (M)	time (h)	phase[b] (% of crystals)
1	0.15	0.15	24	88% C−12% V
2	0.25	0.25	24	55% C−45% V
3	0.35	0.35	24	40% C−60% V
4	0.50	0.50	24	40% C−60% V
5	0.65	0.65	24	39% C−61% V
6	0.75	0.75	24	43% C−57% V
7	0.85	0.85	24	42% C−58% V
8	1	1	24	40% C−60% V
9	0.5	0.5	0.15	98% C−2% V
10	0.5	0.5	1	87% C−13% V
11	0.5	0.5	10	69% C−31% V
12	0.5	0.5	15	52% C−48% V
13	0.5	0.5	24	40% C−60% V
14	0.5	0.5	72	50% C−50% V
15	0.5	0.5	30 days	90% C−10% V
16	0.5	0.5	2 years[c]	40% C−60% V

[a]For all samples, the pH of the biomineralization solutions was set at 9.0 and the temperature was maintained at 30 °C throughout the experimental duration. [b]Abbreviations: V, vaterite; C, calcite. [c]Sample 16 was obtained after 24 h of precipitation under aqueous conditions with the same properties of sample 13 and then was kept in a dry and vacuum condition for 2 years as a control sample.

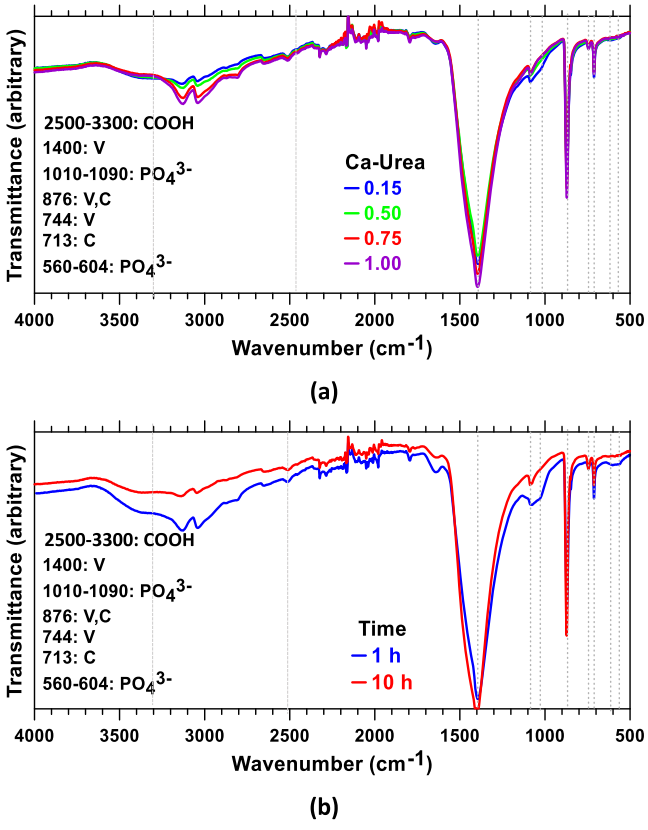

Figure 1. FTIR spectra of bacterially precipitated $CaCO_3$ as a function of (a) calcium and urea concentrations of 0.15, 0.50, 0.75, and 1.00 M at t = 24 h and (b) time at t = 1 h and t = 10 h with calcium and urea concentrations of 0.50 M. All experiments were carried out at 30 °C and an initial pH of 9.

to the carbonate out-of-plane bending (v_2 mode) and in-plane bending (ν_4 mode) vibrations of calcite, respectively.[62−64] It is worth mentioning that the strong vibrational band at 876 cm^{-1} (carbonate out-of-plane bending, v_2 mode) can be assigned to both calcite and vaterite polymorphs, and differentiation between vaterite and calcite polymorphs can be made via the v_4 mode.[65] The vibrational band at 713 cm^{-1} is characteristic of in-plane bending (v_4 mode) for calcite, whereas in vaterite, the same vibrational band is characteristically shifted to 744 cm^{-1}.[65] As shown in the FTIR spectra, no characteristic peaks at 1080 cm^{-1}, attributed to symmetric carbonate stretching (v_1 mode),[64] at 854 cm^{-1}, attributed to carbonate out-of-plane bending (v_2 mode),[63,66] and at 713 and 700 cm^{-1}, attributed to carbonate in-plane bending (v_4 mode),[15] assigned to the aragonite polymorph were detected. The absence of the aragonite phase was further confirmed by XRD results, which will be later discussed.

A vibrational band assigned to the amide-I group was detected at 1655 cm^{-1}, indicating the presence of proteins in the structure of the precipitates.[67] Presence of other organic compounds, such as the vibrational band at 1466 cm^{-1} corresponding to C—C bonds and the vibrational band at 1360 cm^{-1} corresponding to the carboxyl group,[68] was not clearly identified because they could be partially covered by the strongest band of the carbonate group at 1400 cm^{-1}. However, a broad vibrational band corresponding to the O—H stretch of the carboxyl group at 2500−3300 cm^{-1} can be identified for both experimental sets. The vibrational bands assigned to P—O bonds were also identified at 1010−1090 and 560−604 cm^{-1}, which correspond to the PO_4^{3-} asymmetric stretching mode[69,70] and PO_4^{3-} bending mode,[32] respectively, confirming the presence of phosphate-containing components in the structure of the precipitates.

It is worth mentioning that bacterial activity leads to the formation of significant amounts of extracellular polymeric substances (EPSs) that typically surround the bacterial cells and participate in biofilm formation.[71] EPS is a rich matrix of polymers including polysaccharides, proteins, glycoproteins, nucleic acids, phospholipids, and humic acids.[72−74] In particular, polymerized amino sugars, for example, chitin, have been found in *Myxococcus xanthus* EPS,[75] which is well known for its capacity to induce vaterite precipitation.[76]

2.1. Effects of Calcium and Urea Concentrations.

2.1.1. Polymorphic Study. Thermogravimetric analysis (TGA) revealed that the precipitated products for all samples had 94 ± 2% (by mass) of calcium carbonate (dominantly calcite and vaterite as evidenced by powder XRD). The remainder of the composition likely corresponds to organic matter, which decomposes at temperatures ranging between 150 and 450 °C. Figure 2 shows the TGA results for samples 1, 4, and 8 (see Table 1). According to Thiery et al., three modes for decomposition of calcium carbonate have been proposed, coexisting in the ultimate state of carbonation. Mode I (780−990 °C) is most likely associated with the decomposition of well-crystallized calcite. The presence of vaterite and aragonite results in the decomposition of carbonates at lower temperatures corresponding to mode II (680−780 °C), and mode III (550−680 °C) is probably associated with the decomposition of ACC.[77]

Figure 3 shows the powder XRD results for samples 1 to 8 (see Table 1) obtained by applying increasing concentrations of Ca^{2+} and urea from 0.15 M to 1.00 M. According to the standard diffraction patterns of calcite and vaterite (JCPDS file

https://doi.org/10.1021/acsomega.1c00559
ACS Omega 2021, 6, 11988−12003

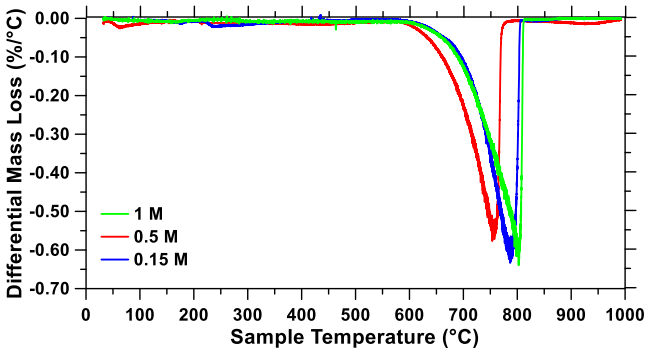

Figure 2. TGA results of bacterially precipitated $CaCO_3$ with equally increasing Ca^{2+} and urea concentrations of 0.15, 0.5, and 1.0 M. Experiments were carried out for 24 h at 30 °C and an initial pH of 9.

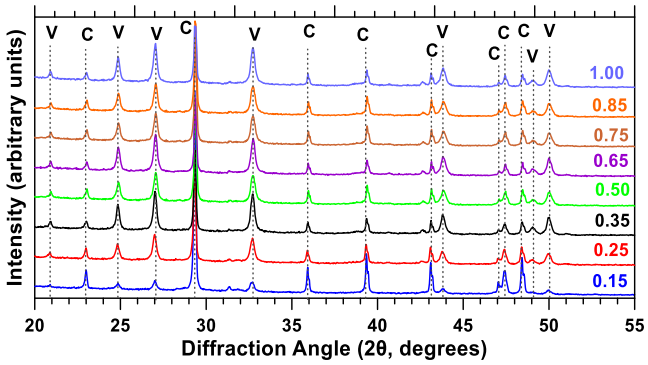

Figure 3. Powder XRD patterns of bacterially precipitated $CaCO_3$ with equally increasing Ca^{2+} and urea concentrations ranging from 0.15 to 1.0 M. Experiments were carried out for 24 h at 30 °C and an initial of pH 9. Herein, C and V represent calcite and vaterite, respectively.

33-0268), the crystalline phase of all samples was composed of a mixture of calcite and vaterite polymorphs. However, the vaterite-to-calcite ratio varied when the concentrations of Ca^{2+} and urea changed. The diffraction peaks of the XRD patterns were relatively sharp, indicating that both calcite and vaterite polymorphs were well crystallized.

The vaterite-to-calcite ratio increased dramatically when the Ca^{2+} and urea concentrations increased from 0.15 to 0.35 M, while it remained relatively constant from 0.35 to 1.00 M (Figure 4). These observations indicate that increasing the Ca^{2+} and urea concentrations up to 0.35 M exerts polymorphic selection on $CaCO_3$ precipitates. It can be deduced that although Ca^{2+} and urea are necessary for calcium carbonate precipitation, increasing the concentrations beyond the capacity of the bacterial activity (corresponding to 0.35 M in the studied case) may not play a significant role in polymorph selection. Nevertheless, morphological variations may be possible.

2.1.2. Morphological Study. Figures 5 and 6 show the scanning electron microscopy (SEM) images of $CaCO_3$ polymorphs for increasing concentrations of calcium and urea. The calcite morphological evolution is shown in Figure 5 for Ca^{2+} and urea concentrations of 0.15, 0.5, and 0.75 M (i.e., samples 1, 4, and 6 in Table 1). At 0.15 M, calcite particles with irregular rhombohedral morphologies were observed (Figure 5a). Crystal faces in most area were smooth. However, partial roughness was observed on some faces. Increasing the Ca^{2+} and urea concentrations to 0.5 M produced two types of

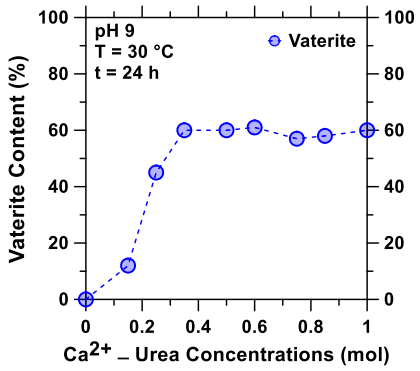

Figure 4. Dependence of bacterially precipitated vaterite content (mass %) on Ca^{2+} and urea concentrations ranging from 0.15 to 1.00 M. Experiments were carried out for 24 h at 30 °C and an initial pH of 9.

calcite particles. The first type is hexagonal-layered structures (Figure 5b), and the second type is a cluster of prismlike structures with an outward orientation (Figure 5c). Figure 5d,e shows calcite particles at calcium and urea concentrations of 0.75 M. It can be seen that at such high concentrations, the morphology is dominated by round and/or oval-shaped polycrystalline subunits, which are fused together.

Our results show that the morphology of the produced polymorphs develops as a function of the Ca^{2+} and urea concentrations. This can be attributed to the necessity of urea for bacterial activity and the consequent production of CO_3^{2-} and organic materials. At lower concentrations (0.15 M), rhombohedral calcite crystals with different sizes are dominant (Figure 5a). As the concentrations of Ca^{2+} and urea increase to 0.50 M, calcite polymorphs with polycrystalline structures appear. These polycrystalline structures consist of relatively large, morphologically well-defined crystallites (Figure 5c). As the concentrations further increase, the size of the crystallites decreases and polycrystalline calcite particles with smaller crystallites form (Figure 5d,e).

The appearance and evolution of the polycrystalline calcite structures can be explained by the classical nucleation and growth theory with respect to the effects of organic materials. At higher concentrations of Ca^{2+} and urea (0.50 M), a larger amount of organic materials is produced. Adsorption of these organic molecules to the surfaces of the crystallites can modify their morphologies and hinder their growth.[6] These temporarily stabilized crystallites tend to aggregate and therefore the growth of the single crystallites through classical ion-by-ion addition is suppressed. Once aggregated, the crystallites are held together by van der Waals forces and/or hydrogen bonds of the adsorbed organic molecules and the inherent dipole–dipole interactions between the individual crystallites, resulting in the formation of polycrystalline particles.[10] As the concentration of Ca^{2+} and urea increases further (e.g., to 0.75 M), the adsorption of the organic macromolecules takes place more rapidly and the growth of the crystallites could be suppressed at an even earlier stage, resulting in the formation of polycrystalline particles with smaller crystallites (Figure 5d,e vs Figure 5b,c, respectively).

Figure 6 shows the morphological evolution of vaterite for samples 4, 6, and 8 (Table 1). Each sample contains a range of particles in terms of size. However, overall, the particle size and porosity tend to decrease when calcium and urea concentrations increase. At a low concentration (i.e., not higher than

https://doi.org/10.1021/acsomega.1c00559
ACS Omega 2021, 6, 11988−12003

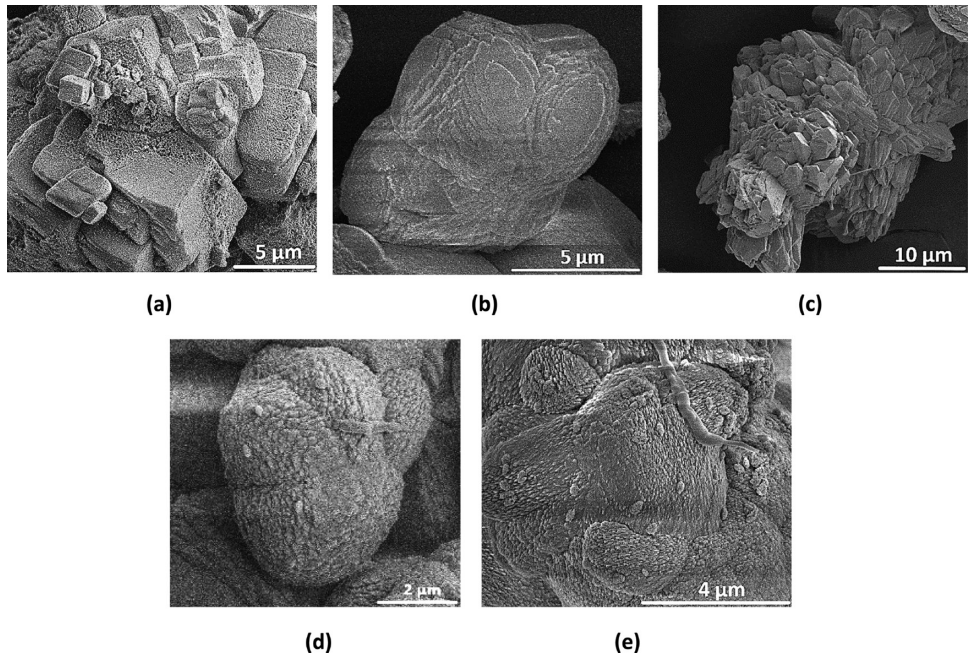

Figure 5. SEM images of morphological evolution of calcite particles at 30 °C, initial pH of 9, and calcium and urea concentrations of (a) 0.15 M, (b,c) 0.50 M, and (d,e) 0.75 M.

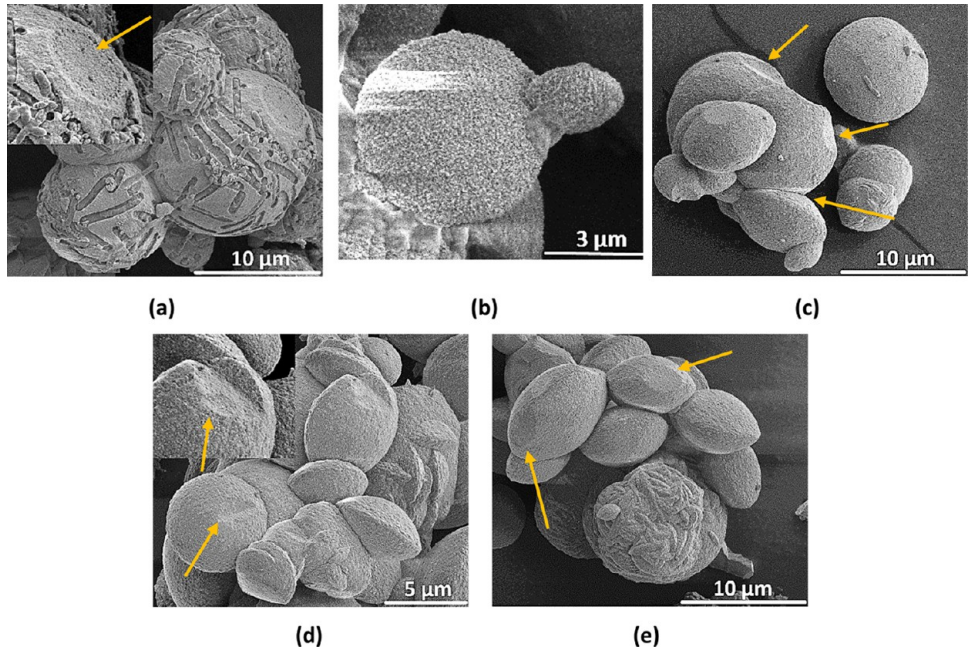

Figure 6. SEM images of morphological evolution of vaterite particles at 30 °C, an initial pH of 9, and calcium and urea concentrations of (a,b) 0.50 M, (c) 0.75 M, and (d,e) 1.00 M.

0.5 M), vaterite particles are mostly governed by a spherical profile (see Figure 6a). However, at higher concentrations from 0.5 M, vaterite particles with an oval shape appear (see Figure 6c at 0.75 M) and gradually dominate the particle morphology at 1.00 M (see Figure 6d,e).

Comparing the surface and subsurface structures of the spherical and oval-shaped vaterite particles (shown in the insets of Figure 6a,d), it can be seen that the structure of oval-shaped particles obtained at higher concentrations of Ca^{2+} and urea is much more compacted than the spherical particles formed at lower concentrations. Even the spherical particles obtained at higher concentrations (shown in Figure 6d with an arrow) exhibit a more compacted texture compared to the spherical particles obtained at lower concentrations. Since the physical, chemical, and mechanical properties of minerals depend on their microstructure, one can speculate that the vaterite particles produced at higher concentrations of Ca^{2+} and urea could have higher density, lower chemical reactivity, and higher strength when carrying mechanical loads in specific applications. This can also be interpreted from the visual observation of SEM images. The number of broken spherical vaterite particles observed at lower concentrations of Ca^{2+} and

https://doi.org/10.1021/acsomega.1c00559
ACS Omega 2021, 6, 11988−12003

urea was much more than those observed at higher concentrations, and no broken oval-shaped particle was observed even at the lowest concentration at which these particles were detected (i.e., 0.50 M). These observations indicate that the vaterite particles produced at lower concentrations of Ca^{2+} and urea had lower mechanical resistance to grinding. This could be attributed to the higher incorporation of organic materials into the vaterite structure at higher concentrations or/and higher density of the vaterite particles because of the higher incorporation of the calcium and carbonate ions into their structural skeleton.

Figure 6c,e shows some depressions on the body of the vaterite particles indicating that the growth of one particle can be terminated in one direction by the growth of adjacent particles. These particles can stay attached to each other or smaller particles can be detached from the larger ones leaving their footprints on the body of the larger particles. As the concentrations of Ca^{2+} and urea increase, the number of depressions also increases while the size of depressions decreases, indicating that the rate of vaterite precipitation increases on raising the Ca^{2+} and urea concentrations. Perfect spheres and ovals can form if no other particles hinder their growth such as those observed at lower concentrations (Figure 6a).

2.2. Time-Dependent Biomineralization Kinetics. *2.2.1. Kinetics of the Biomineralization Solution and Polymorphic Study.* The interaction of urea hydrolysis and calcium carbonate precipitation was studied by continuously monitoring the evolution of pH and electrical conductivity (EC) over a time period of 30 days. The EC value reflects the number of electrolytic ions in a solution. Hence, its evolution could demonstrate the changes in magnitude and rate of ureolytic activities. Furthermore, interactions between electrolytes released by bacterial ureolytic activities and the electrolytes present in the biomineralization solution could also be evidenced by monitoring the pH and EC evolution.

Figure 7 shows the EC and pH evolution profiles over a time period of 30 days. The conductivity profile showed a sudden

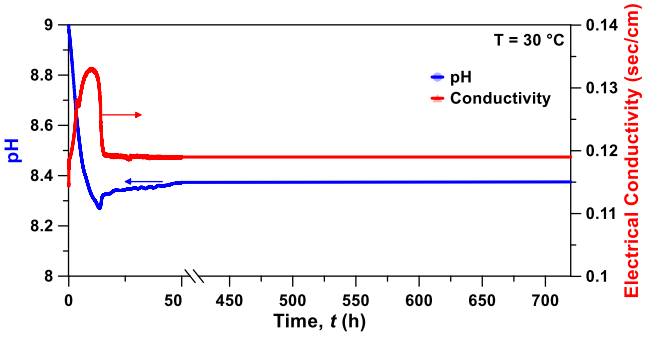

Figure 7. pH and EC profiles measuring the continuous change in pH and EC of the biomineralization solution in a time period of 720 h at an initial pH of 9, Ca^{2+} and urea concentrations of 0.5 M, and 30 °C.

initial increase from t = 0 (addition of bacteria) to t = 0.15 h, which indicates that the bacteria started hydrolysis of urea right after being applied to the solution. The conductivity continuously increased with a nearly constant rate until it reached the maximum point at t = 11 h. After this point, a gradual decrease in conductivity was observed until t = 16 h, which was followed by a constant value until the end of the experiment at t = 30 days.

After addition of the bacteria to the solution, the bacterial ureolytic activity was expected to initially increase the local pH in the proximity of the bacterial cells due to the hydrolysis of urea and release of hydroxyl ions.[20] However, in our study, the pH value interestingly decreased, reaching the minimum value of 8.27 at t = 14 h and then increased within the next 2 h reaching a value of 8.33 at t = 16 h and remained almost constant until t = 30 days. Such a decrease in the pH value can be due to the $Ca(OH)_2$ complexation.[78] In alkaline solutions that contain Ca^{2+} and OH^-, in addition to $Ca(OH)_2$, formation of $CaOH^+_{(aq)}$ is also significant.[79] In our experiment, we set the initial pH at 9, which is the optimum pH for the *S. pasteurii* ureolytic activity, by addition of NaOH to the solution. Addition of NaOH, in turn, provides a favorable condition for $Ca(OH)_2$ complexation. Pallagi et al.[78] examined the solubility of $Ca(OH)_2$ in a wide range of NaOH concentrations, including under extremely basic conditions. In the presence of NaOH (up to 1 M concentration), the solubility of $Ca(OH)_2$ increases. Therefore, in these systems, formation of $Ca(OH)_{2(aq)}$ in sufficient quantities seems unlikely compared to the formation of complex $CaOH^+_{(aq)}$.[78] Hydroxyl ions produced by the bacterial activity along with those released by the addition of NaOH undergo $Ca(OH)_2$ complexation, and as a result, the pH value decreases at the beginning of the bacterial addition despite urea hydrolysis. Setting the solution's pH higher than the neutral value also provides a supersaturation condition and facilitates the precipitation of calcium carbonate. Therefore, precipitation occurs shortly after the application of bacteria and production of the CO_3^{2-} ions as a result of urea hydrolysis. Later, as precipitation of calcium carbonate proceeds, the consumption of calcium ions results in dissociation of $Ca(OH)_2$ and $CaOH^+_{(aq)}$ and release of the hydroxyl ions, leading to a rise in the pH level until t = 24 h. However, the rate of increase in the pH value decreases from t = 16 h to t = 24 h and shows almost a constant value after t = 24 h till the end of the experimental duration at t = 720 h, indicating an equilibrium status.

Figure 8 shows the powder XRD patterns for samples 9 through 15 obtained in the time intervals listed in Table 1. It

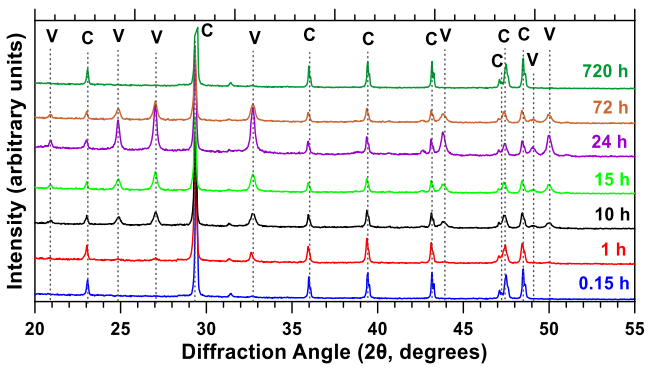

Figure 8. Powder XRD patterns of bacterially precipitated $CaCO_3$ as a function of time. Experiments were carried out at 30 °C, an initial pH of 9, and for time intervals at t = 0.15, 1, 10, 15, 24, 72, and 720 h. Herein, C and V represent calcite and vaterite, respectively.

can be seen that the crystalline phases of all samples were composed of a mixture of calcite and vaterite polymorphs. However, the vaterite-to-calcite ratio varied at different time intervals. The sharpness of the diffraction peaks for both polymorphs increased as time passed indicating that the degree

https://doi.org/10.1021/acsomega.1c00559
ACS Omega 2021, 6, 11988−12003

of crystallinity for both calcite and vaterite polymorphs increases with time and the polymorphs obtained at later time intervals developed into better crystalline structures.

The results obtained from the powder XRD test showed that precipitates collected at t = 0.15 h contained about 98% calcite and 2% vaterite and those collected at t = 1 h contained about 87% calcite and 13% vaterite. At t = 10 h, 70% calcite and 30% vaterite were collected and at t = 15 h, this amount reached 50% for each polymorph. The percentage of vaterite gradually increased with time and reached the maximum value of 60% over 40% of calcite at t = 24 h. After this time, the vaterite-to-calcite ratio gradually decreased showing 50% calcite and 50% vaterite at t = 72 h and reached nearly 10% vaterite and 90% calcite at t = 30 days (Figure 9).

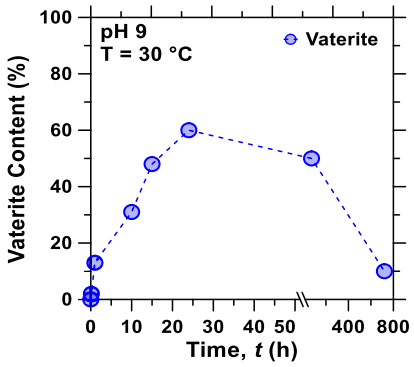

Figure 9. Dependence of bacterially precipitated vaterite content (mass %) on time from t = 0.15 h to t = 720 h (30 days). Experiments were carried out at 30 °C, an initial pH of 9, and Ca^{2+} and urea concentrations of 0.50 M.

The gradual decrease in the calcite content and increase in the vaterite content up to t = 24 h and a gradual increase in the calcite content and decrease in vaterite content after t = 24 h under aqueous conditions indicate that calcite formation can occur prior to, after, or concurrent with vaterite formation. These observations also suggest that calcite and vaterite particles can form independently, which rules out Ostwald's law of stages for the first 24 h of the precipitation under the experimental conditions of this study. As supersaturation changes throughout the experimental timescale, various pathways become available for the $CaCO_3$ nucleation and crystallization to proceed. At the onset of the experiment, supersaturation increases to the solubility limit of the calcite polymorph due to the production of CO_3^{2-} and NH_4^+ and the organic macromolecules secreted by the bacterial activity. However, the supersaturation level is still lower than the supersaturation of the metastable phase, vaterite. Therefore, the dominant phase at the first hour of the precipitation is calcite coexisting with a small portion of vaterite polymorph. The coexistence of stable and metastable phases was also reported by Johnston et al.,[80] indicating the existence of anhydrous and hydrated $CaCO_3$ crystalline phases under the typical laboratory conditions, which favored the formation of the thermodynamically stable phase, calcite. Brečević and Nielsen,[81] Radha et al.,[82] and Gebauer et al.[45] also reported the existence of amorphous phases as well as the calcite polymorph under the same laboratory conditions.

As the solute concentrations increase to the solubility limit of the metastable phase, the degree of supersaturation becomes high enough that the metastable phase (vaterite) becomes increasingly predominant. Such a high supersaturation leads to a decrease in energy barriers and therefore multiple pathways become thermodynamically available.[83] Hence, at higher supersaturation, while the dominant phase is the metastable phase (vaterite), the stable phase (calcite) still forms. This phenomenon can be interpreted from the EC profile (Figure 7) as well. The conductivity is the sum of contribution of all ions that are present in the solution. As the concentration of the ions increases, conductivity also increases accordingly. However, the ions contribute differently to the EC based on their mobility and the electrical unit charges.[84] At t = 10 h, the conductivity profile shows the maximum value indicating that the supersaturation reached the metastable phase supersaturation level. This can be supported by the XRD results (Figure 8) showing that the vaterite ratio increases as time passes and surpasses the calcite ratio at t = 15 h and continues to increase until t = 24 h.

Another phenomenon contributing to the vaterite formation is the production of a high amount of EPS when the bacterial activity reaches its maximum level. It has been reported that the ratio between the calcite and vaterite polymorphs seems to be related to the abundance and the nature of EPS, especially the nature of the amino acids. At high EPS concentrations, amino acids—mainly glycine[85] and aspartic and glutamic acids[54] —induce vaterite precipitation and stabilization although the calcite polymorph still formed. The role of the carboxyl group is also probably critical because the bacterial outer structures associated with peptidoglycan commonly contain carboxyl groups.[54] With time, supersaturation decreases due to consumption of Ca^{2+} and CO_3^{2-} as a result of the calcium carbonate precipitation. The bacterial activity also decreases due to the urea (source of CO_3^{2-}) consumption. The production of EPS and other organics also diminishes due to the lower bacterial activity and incorporation of organic molecules into the structure of the $CaCO_3$ crystals. The EC profile shows a constant value from t = 16 h till the end of the experiment, indicating that the concentration of electrolytes in the biomineralization solution has reached an equilibrium (Figure 7). However, the vaterite-to-calcite ratio continues to increase until t = 24 h (40% calcite and 60% vaterite), then shows a gradual decrease reaching 50% calcite and 50% vaterite at t = 72 h, and continues to decrease reaching 1:9 after 30 days. These observations indicate that there is a gradual phase transformation from vaterite to calcite polymorphs after t = 24 h; however, this gradual transformation was only observed for the samples under aqueous conditions with continuous stirring. The comparison between composition of the samples stored under dry conditions for almost 2 years (sample 16 in Table 1) and the samples obtained under aqueous conditions after 30 days reveals that transformation from the metastable phase, vaterite, to the stable phase, calcite, takes place only if humidity is present.

Figure 10 shows the newly formed nanocalcite rhombohedrons on the body of a vaterite particle at t = 24 h. It can be interpreted from the EC profile (Figure 7) and Figure 10 that as supersaturation decreases from t = 10 h and reaches the solubility limit of the calcite polymorph between t = 16 h and t = 24 h, new calcite nuclei form and begin to grow heterogeneously on the body of the vaterite particle (Figure 10). The growth of these calcite nuclei eventually results in the consumption and depletion of Ca^{2+} in the solution. As the Ca^{2+} concentration decreases in the proximity of the newly formed calcite nuclei, calcite nuclei continue to grow at the expense of

https://doi.org/10.1021/acsomega.1c00559
ACS Omega 2021, 6, 11988−12003

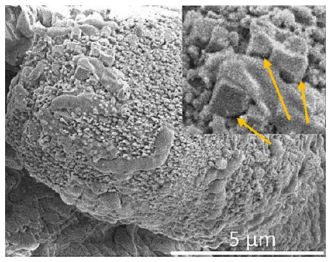

Figure 10. SEM image of newly formed calcite particles on the body of the vaterite particle at t = 24 h, 30 °C, an initial pH of 9, and calcium and urea concentrations of 0.5 M.

vaterite dissolution. The continuous growth of the calcite particles on the body of the vaterite particles prevents supersaturation from reaching the solubility limit of the vaterite polymorphs. Therefore, vaterite particles continue to dissolve providing required calcium ions for the calcite growth evidencing that although the EC profile shows a constant value after t = 16 h, phase transformation continues at the microscale level.

These observations also indicate that the vaterite-to-calcite transformation even after t = 24 h—at least under the conditions studied in this research work—proceeds via dissolution of the less stable phase (vaterite) and crystallization of the more stable phase (calcite) from the solution as suggested by the solvent-mediated transformation pathway.

The newly formed calcite particles can also provide an insight into the calcite growth process suggesting that the calcite growth proceeds via ion-by-ion addition to the primary nucleus as proposed by the classical nucleation and growth theory. A similar conclusion was drawn by Hu et al. who suggested that ACC nanoparticles do not serve as direct precursors to the calcite particles as suggested by the nonclassical nucleation and growth theory, rather calcite nucleation takes place by an ion-by-ion addition from the solution to the calcite nuclei, which formed on the carboxyl-terminated organothiol self-assembled monolayers (SAMs), an ion-by-ion addition from the solution, and also ion-by-ion addition as a result of the ACC dissolution in the case of hydroxyl-terminated SAM.[86] It is worth mentioning that the very early stage of the nucleation could not be captured easily due to the lack of advanced imaging tools and so far the transformation of an amorphous particle into a crystal has not been directly observed, rather it has been inferred from the sequence of events, for example, ACC formed first and was eventually replaced by one of the crystalline phases. In addition, nearly all previous studies in which ACC formed before the formation of more stable phases were carried out at supersaturation well in excess of the solubility limit of

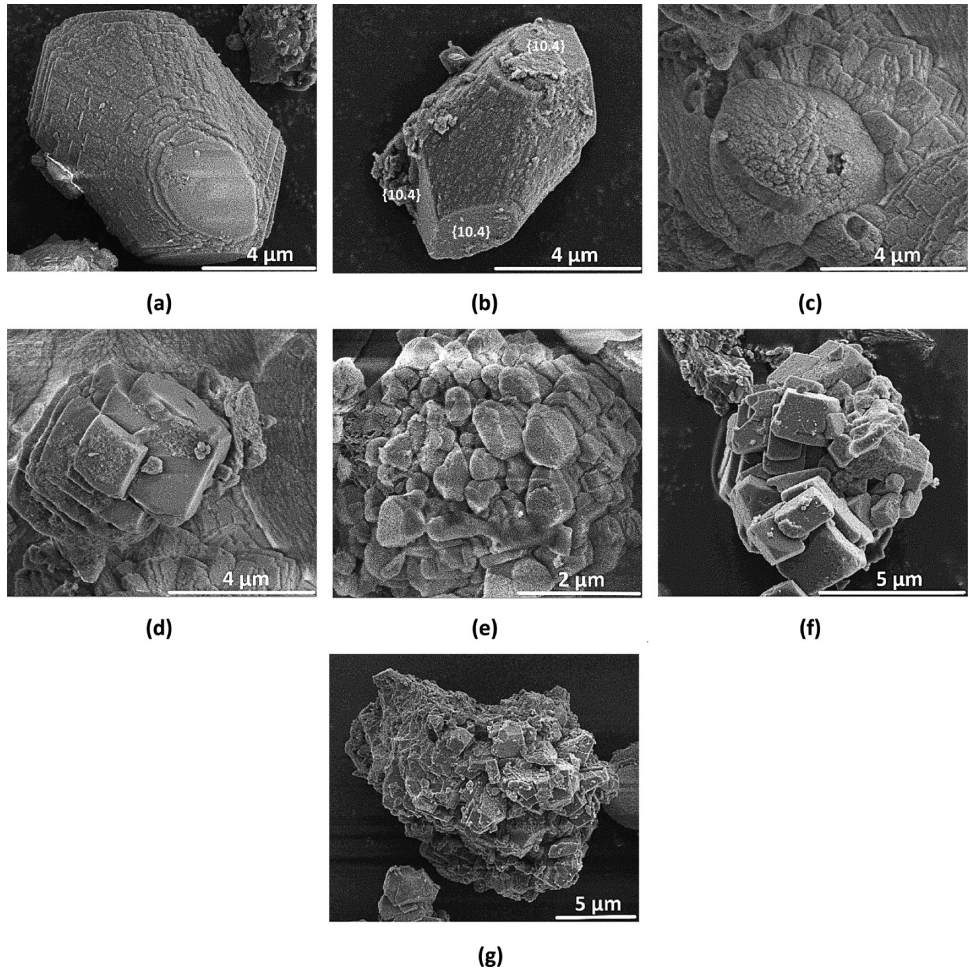

Figure 11. SEM images of morphological evolution of calcite particles at 30 °C, an initial pH of 9, calcium and urea concentrations of 0.5 M, and time intervals of (a–e) t = 1 h and (f,g) t = 10 h.

https://doi.org/10.1021/acsomega.1c00559
ACS Omega 2021, 6, 11988–12003

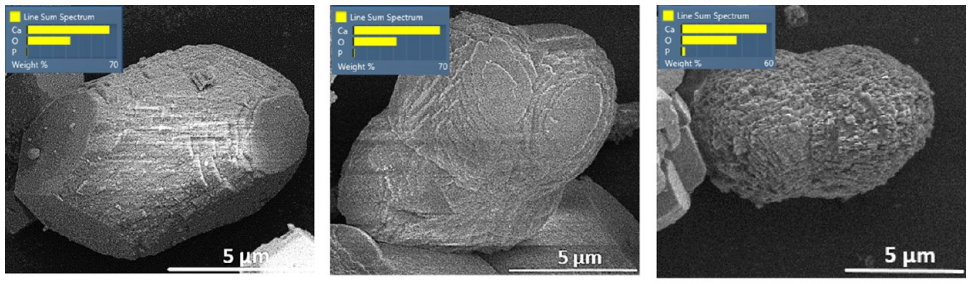

Figure 12. SEM images of morphological evolution of calcite particles at (a) time intervals of t = 1 h and calcium and urea concentrations of 0.5 M, (b) time intervals of t = 24 h and calcium and urea concentrations of 0.5 M, and (c) time intervals of t = 24 h and calcium and urea concentrations of 0.75 M. Experiments were carried out at 30 °C and an initial pH of 9.

ACC,[46,49] and at such a high supersaturation, it is common that ACC forms first prior to other more stable phases.[86] Our results indicate that no matter the early stage of the nucleation takes place by classical ion-by-ion addition or nonclassical prenucleation clusters, the crystallization events proceed via ion-by-ion addition for the calcite polymorph at the onset of the experiment and during the phase transformation stage. It is worth mentioning that at the phase transformation stage, dissolution of the vaterite provides the necessary Ca^{2+} sources for recrystallization of the calcite.

2.2.2. Morphological Study. Figures 11 and 12 show the SEM images of $CaCO_3$ polymorphs at the time intervals from 0.15 h to 30 days. Figure 11 shows the calcite morphological characteristics at t = 1 h and t = 10 h. In the first hour after the addition of the bacterial cells to the solution, a distinct range of calcite particles formed in terms of morphological features (Figure 11a−e). A hexagonal-layered structure can be seen in Figure 11a which in some cases was elongated at the crystallographic c-axis (Figure 11b). Figure 11c shows an interesting fried egglike structure composed of a spherical core mass and rhombohedral sheets accumulated in the surrounding regions. Figure 11d shows rectangular crystals of calcite with smooth faces sitting on top of each other, and Figure 11e shows a calcite structure formed of an imperfect spherical cluster made of imbricated rhombohedrons. As time passed, the calcite particles tended to aggregate and mostly displayed polycrystalline structures with regular (Figure 11f) or irregular (Figure 11g) crystallite orientations. At t = 24 h, calcite particles exhibited the same morphological features as sample 4 (Figure 5b,c) with calcium and urea concentrations of 0.5 M under the same experimental conditions (Table 1).

The time-dependent morphological evolution of the calcite polymorph can be explained via the classical nucleation and growth theory with respect to the organic molecule effect. At t = 1 h, the concentration of organic compounds secreted by bacteria is not high enough to induce the formation of the polycrystalline structures (as those obtained at the Ca^{2+} and urea concentrations higher than 0.35 M). Therefore, adsorption of the organic molecules to the surface of the crystals takes place at a very slow rate such that the growth of the calcite particles still proceeds via classical ion-by-ion addition to the existing individual crystal. However, adsorption of the organic molecules to the crystal faces still exerts some control on the individual crystal morphologies. A closer view of the structure of the calcite particles in Figure 11a shows the expression of the c-axis. The c-axis of calcite is either purely anionic or cationic and consists of alternate layers of Ca^{2+} and CO_3^{2-}[6,87] and therefore is not usually exposed.[88] Depending on the geometry of the organic molecules and the chemistry and orientation of their functional groups,[89,90] the anionic or cationic faces can be stabilized. Adsorption of organic molecules with negative or positive charges on the respective faces may direct the final orientation of the calcite crystals by lowering the surface energy and inhibiting the growth in the respective direction resulting in the exposure of the faces parallel to the c-axis and consequently unusual crystal morphologies.[88]

As shown in Figure 11b, the calcite crystal is elongated at the crystallographic c-axis with three {10.4} faces on each end of the crystal (one of the {10.4} faces is located at the other side of the particle). This further indicates that organic molecules interact preferentially with the faces parallel to the c-direction[10] and continuing this interaction results in the further exposure of those faces and further elongation of the crystals. Wang et al.[10] observed the same morphological features for calcite crystals in the presence of sodium citrate as an organic additive. They attributed this effect to the presence of citrate with three —COO— groups. The —COO— groups can interact with the Ca^{2+}-containing surface of calcite crystals through electrostatic and/or bonding interactions and induce formation of the elongated calcite particles with {10.4} faces.[91−93] Our FTIR results (Figure 1b) also show that the intensity of the peaks assigned to the carboxyl and phosphate groups is higher at the onset of the experiment (t = 1 h) compared to the rest of the experimental timescales. Therefore, it is not surprising that formation of the elongated calcite particles is more common at this time of the experiment.

As time passes and the bacterial activity reaches its maximum capacity, a large amount of organic molecules is produced and secreted to the surrounding environment. Figure 12 shows the morphological evolution of the calcite polymorphs with respect to the availability of the organic materials in the surrounding environment. At t = 24 h (Figure 12b), the concentration of the organic molecules in the biomineralization solution is high enough compared to that at t = 1 h (Figure 12a) to hinder the growth of the individual crystals and induce formation of the polycrystalline structures. Therefore, a number of hexagons as seen at t = 1 h fuse to each other to form an aggregated structure (Figure 12b). As the concentration of the organic material further increases with the increasing urea concentration from 0.50 M to 0.75 M at t = 24 h, the adsorption of the organic molecules to the surface of the calcite crystals takes place more rapidly and the growth of the crystallites gets suppressed at the earlier stage resulting in the formation of polycrystalline particles with smaller crystallites (Figure 12c).

https://doi.org/10.1021/acsomega.1c00559
ACS Omega 2021, 6, 11988−12003

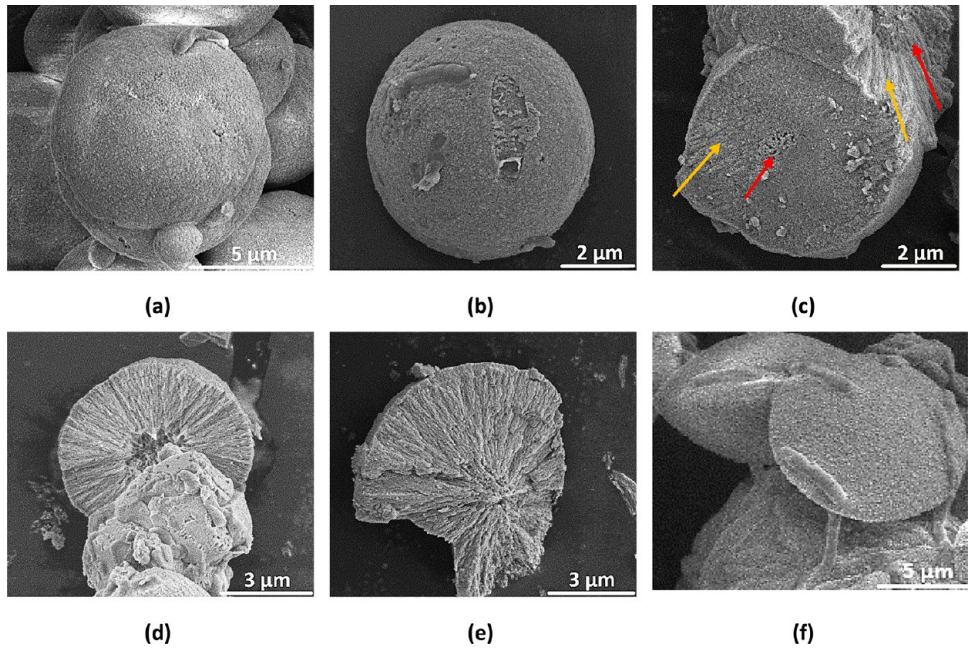

Figure 13. SEM images of morphological evolution of vaterite particles at 30 °C, an initial pH of 9, calcium and urea concentrations of 0.5 M, and time intervals of (a) t = 1 h, (b−e) t = 10 h, and (f) t = 24 h.

A closer view of the FTIR profiles for both experimental sets (Figure 1) shows that although the overall intensity of the vibrational bands assigned to the organic compounds increased with the increase in the vaterite-to-calcite ratio, the vibrational bands corresponding to the carboxyl group at 2500−3300 cm^{-1} and the phosphate group at 1010−1090 cm^{-1} showed an opposite behavior, inferring that carboxyl and phosphate groups play a role in $CaCO_3$ polymorph selection by inducing the calcite formation as well as in controlling the morphological features of the calcite particle by stabilizing the crystal faces parallel to the c-axis leading to the unusual elongated crystals.

The presence of the P element in the structure of the calcite particles was also examined by EDS elemental mapping. The corresponding EDS results for each calcite structure are shown in Figure 12. The results indicate that incorporation of the phosphorus-containing organic molecules into the calcite structure increases at higher concentrations of the organic compounds, regardless of the decrease in the overall calcite content. These observations provide a strong support for the mechanism proposed for the calcite morphological evolution from single crystals to polycrystalline structures. At higher concentrations of the organic compounds, adsorption of the organic molecules to the surface of the calcite crystals takes place more rapidly and the growth of the crystallites retards at the earlier stage resulting in their aggregation. The aggregation of the crystallites further traps the organic molecules; therefore, the EDS results show higher incorporation of the P element into the calcite structures at higher concentrations of the organic molecules.

Figure 13 shows the vaterite morphological evolution at t = 1 h, t = 10 h, and t = 24 h. Vaterite particles showed a spherical profile up to 24 h, and at t = 24 h, oval-shaped vaterite particles appeared (Figure 13f). At t = 1 h, the majority of the vaterite particles exhibited a binary structure (Figure 13a). However, as time passed, perfect fibro-radial spheres dominated (Figure 13b). Incomplete and broken particles shown in Figure 13c−e show the cross-sectional view of the interior structure of vaterite. Two distinguishable zones can be specified (Figure 13c) showing a spongy texture in the core of the vaterite sphere (red arrows) and a more compacted texture toward the edges (yellow arrows). Figure 13d,e further shows that each fibro-radial sphere was composed of two concentric rings. The outer ring was composed of radially aligned nanofibers extended to the center of the sphere. These nanofibers displayed different lengths and shorter fibers failed to reach the center of the sphere, leaving an inner ring with a significantly porous texture, or in some cases, a hollow cavity. EDS elemental mapping of the broken vaterite crystal showed a small trace of the S element, implying that sulfur-containing organic molecules may induce vaterite precipitation. Unlike the inner structure, the outer surface of vaterite particles were relatively smooth and uniform as shown in Figure 13b.

2.3. Physical and Chemical Association of Bacterial Cells with $CaCO_3$ Polymorph Selection and Morphological Evolution. Nucleation and growth of biomineral materials are controlled by a variety of parameters including the biological effects of living organisms and the presence of organic materials in the surrounding environment.[52] The presence of living organisms itself, on the other hand, enhances the challenges over controlling factors during the biomineralization process.[53] Involvement of the bacterial cell wall as a nucleation site in bacterially induced $CaCO_3$ precipitation has been recently investigated. It has been believed that bacterially induced $CaCO_3$ precipitation is driven primarily by urea hydrolysis.[16] However, bacterial cell walls are also expected to possess negatively charged units, which likely result in the transportation of Ca^{2+} ions toward the cell surface facilitating $CaCO_3$ nucleation at the cell surface.[25,34]

In both experimental sets of the current study, a close association of the bacterial activity with the calcium carbonate precipitation process was observed. However, the population of the bacterial cells physically associated with the vaterite

https://doi.org/10.1021/acsomega.1c00559
ACS Omega 2021, 6, 11988−12003

particles was significantly greater than that associated with the calcite particles.

Figure 14a,b (taken at t = 24 h and Ca^{2+} and urea concentrations of 0.50 M) shows vaterite particles with a significant population of embedded bacterial cells on the surface of the particles, whereas in the case of calcite, bacterial cells were mostly found in the bulk medium close to the calcite particles or at the conjunction of the calcite crystallites in the polycrystalline structures (Figure 14c). Physical association of the bacterial cells with the morphological features of the vaterite particles can be also evidenced as shown in Figure 14a,b. Figure 14a shows a group of bacterial cells collaborated to form a single vaterite sphere; in such a case, nucleation of vaterite particles took place in the proximity of the bacterial cells. Therefore, bacterial cells still preserved their mobility and left the impression of their existence on the body of the vaterite particle (yellow arrows). Figure 14b, however, shows that the spherical growth of the vaterite crystals took place in aggregation with the bacterial cells resulting in the death of bacteria and leaving a rod-shaped vaterite particle that resembled the initial shape of the bacteria.

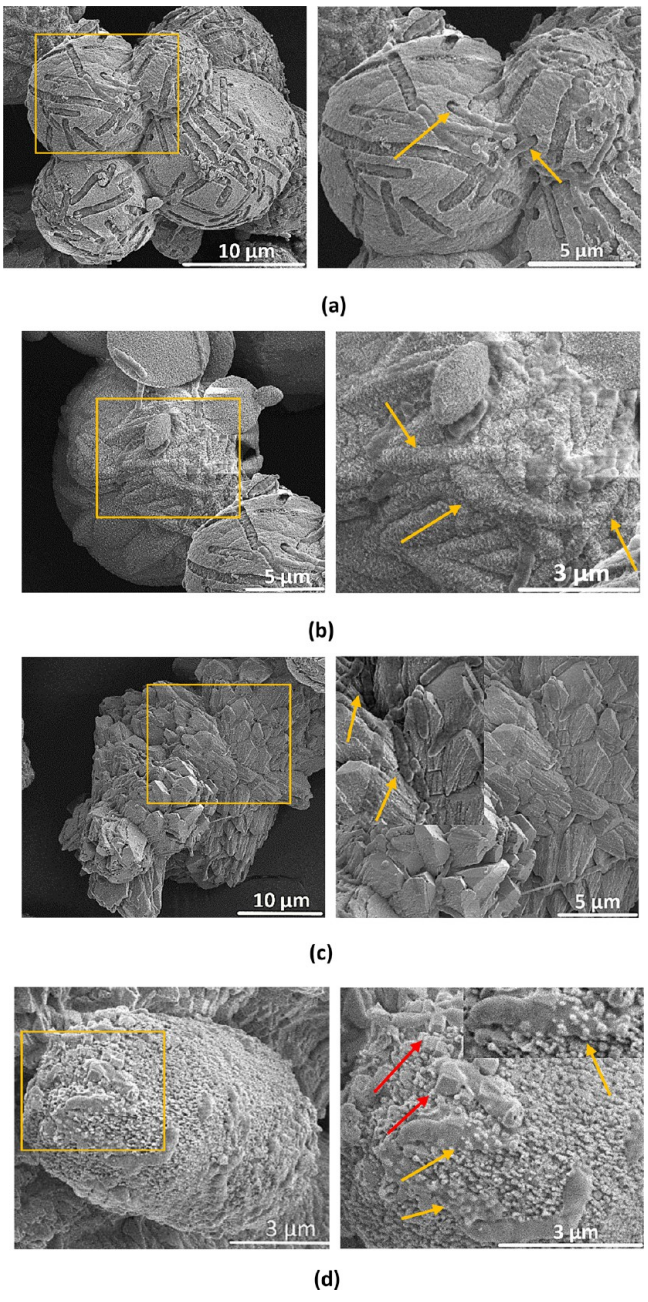

Figure 14. SEM images of association of bacterial cells with $CaCO_3$ precipitation at 30 °C, an initial pH of 9, calcium and urea concentrations of 0.5 M, and t = 24 h. (a) Bacterial cells embedded on the surface of vaterite particles, (b) growth of the vaterite crystals in aggregation with the bacterial cells, (c) bacterial cell accumulation at the conjunction of the calcite crystallites in polycrystalline structures, and (d) nucleation of the vaterite particles on the body of the bacterial cells (yellow arrows) and newly formed calcite rhombohedrons on the body of the vaterite particles (red arrows).

Figure 14d, taken at t = 24 h and Ca^{2+} and urea concentrations of 0.50 M, further sheds light on the $CaCO_3$ biomineralization process at the cellular length scale. Two distinct phenomena are evident: first, nucleation of the vaterite nanoparticles on the body of the bacterial cells (Figure 14d, yellow arrows); second, the appearance of the calcite rhombohedrons on the body of the vaterite particles (Figure 14d, red arrows). These two phenomena indicate that $CaCO_3$ biomineralization can be identified in two spatial domains: the nanoscale neighborhood of the bacterial cell surface and the bulk medium. Our results suggest that calcite formation mostly takes place in the latter domain while it is influenced by the metabolic activity of bacteria. The ureolytic activity of bacterial cells contributes to the formation of the calcite particles by the production of CO_3^{2-}, increasing the local pH in proximity of the bacterial cells, and secretion of the EPS into the bulk medium. However, physical contribution of bacterial cells in nucleation and crystallization of calcite polymorphs was not elucidated under the experimental conditions of this study. The appearance of the calcite rhombohedrons on the body of the vaterite particles via the solvent-mediated transformation pathway further indicates that nucleation and crystallization of calcite polymorphs may be controlled by biochemical effects of the bacterial activity and chemistry of the bulk medium. Formation of the vaterite polymorph, on the other hand, is controlled by both events, the physical and biochemical properties of the bacterial cells as well as the chemical properties of the bulk medium. The presence of nanosized vaterite particles on the bacterial cell surface (Figure 14d, yellow arrows) and the observations made to study the vaterite morphological evolution (Figure 14a,b) provide a strong support for the theory that the bacterial cell surface can serve as a nucleation site for $CaCO_3$ precipitation.

A similar argument was used by Ghosh et al.[16] to explain the initial stages of $CaCO_3$ precipitation in the micro- and macroenvironments of the bacterially induced $CaCO_3$ precipitation system. In a urea-containing medium with dead bacterial cells, rhombohedral crystalline (calcite) particles formed, while in the urea-containing medium with live bacterial cells, precipitates in the form of microspheres (vaterite) with a significant population of embedded bacterial cells were observed. These results suggested that precipitation in the presence of dead cells were chemically controlled, whereas in the presence of live cells, precipitation is likely both chemically and biochemically controlled.[16] Mitchell and Ferris[37] also studied the influence of bacterial cells on the nucleation of $CaCO_3$ in which a bacteria-free urease solution was compared to a bacteria-containing medium. The authors reported that the bacteria-free urease solution showed similarities with the bulk chemical precipitation, while

https://doi.org/10.1021/acsomega.1c00559
ACS Omega 2021, 6, 11988−12003

$CaCO_3$ precipitation in the bacteria-containing medium was distinctly different. This suggests that the presence of bacteria itself exerts polymorphic and morphological effects on the $CaCO_3$ precipitates.

These observations along with our results suggest that precipitation of vaterite polymorphs and in some cases (Figure 14b) the morphological features of vaterite particles were mostly controlled by the physiochemical and biochemical properties of the bacterial cell as well as the chemical properties of the bulk medium. However, the precipitation of calcite polymorphs was mostly controlled by the two latter events (i.e., biochemical properties of bacterial cells and chemistry of the bulk medium) and physical properties of the bacterial cells did not play a considerable role in selection of the calcite polymorph and its morphological features.

3. CONCLUSIONS

The underlying mechanism that controls polymorph selection and morphological features of the bacterially precipitated $CaCO_3$ is still unclear and controversial. The dynamics of nucleation, growth and crystallization, and transformation of metastable phases also require a more detailed investigation. The presence of living organisms itself, on the other hand, enhances the challenges over controlling factors during the biomineralization process. In an effort to elucidate some of these controversies, this study employed *S. pasteurii* in two experimental sets to study the effects of Ca^{2+} and urea concentrations on the polymorph selection and morphological evolution of the bacterially precipitated $CaCO_3$ and also to study the $CaCO_3$ crystallization process at the microscale by monitoring the pH and EC of the biomineralization solution over a time period of 30 days. The following conclusions can be drawn from this study:

- Increasing the Ca^{2+} and urea concentrations up to a certain level (i.e., 0.35 M in this study) exerts polymorphic selection on $CaCO_3$ precipitates by inducing vaterite formation over calcite and increasing the concentrations further did not show any considerable effect on the vaterite and calcite percentages.
- Morphology of the produced polymorphs develops as a function of the Ca^{2+} and urea concentrations. The morphology of calcite evolves from single crystal to polycrystalline structures and the morphology of vaterite evolves from spherical to oval-shaped structures on increasing the concentrations of Ca^{2+} and urea.
- The structure of oval-shaped vaterite particles obtained at higher concentrations of Ca^{2+} and urea is much more compacted than the spherical particles formed at lower concentrations, indicating that vaterite particles produced at higher concentrations could have higher density, lower chemical reactivity, and higher strength when carrying mechanical loads in specific applications.
- The time-resolved experiment shows that the vaterite-to-calcite ratio increases up to 24 h reaching 60−40% due to bacteria-induced polymorph selection and after that decreases reaching 10−90% at 720 h under aqueous conditions due to phase transformation after 24 h (when EC and pH profiles showed a constant value).
- Transformation of the metastable phase, vaterite (at least biomineralized vaterite under the studied conditions), to the stable phase, calcite, takes place only if humidity is present.
- The phase transformation, from vaterite to calcite, after 24 h takes place via a solvent-mediated transformation pathway and crystallization of calcite particles proceeds at the expense of vaterite dissolution.
- The exact mechanism of nucleation for calcite and vaterite polymorphs could not be elucidated under the experimental conditions of this study; however, calcite and vaterite particles can form independently at the onset of the experiment, which rules out Ostwald's law of stages for the first 24 h of the precipitation under the experimental conditions of this study.
- Carboxyl and phosphate groups could play a role in $CaCO_3$ polymorph selection by inducing calcite formation and in controlling the morphological features of the calcite particles by inducing the crystals, which were elongated in the *c*-direction. Sulfur-containing organic molecules, on the other hand, induced formation of the vaterite polymorph.
- Precipitation of vaterite polymorphs and in some cases the morphological features of vaterite particles are mostly controlled by the physiochemical and biochemical properties of the bacterial cell as well as the chemical properties of the bulk medium. However, the precipitation of calcite polymorphs is mostly controlled by the biochemical properties of bacterial cells and chemistry of the bulk medium; the physical properties of the bacterial cells do not play a considerable role in the selection of the calcite polymorph and its morphological features.

These findings provide useful information suggesting that nucleation, growth, and crystallization of calcium carbonate in biological systems do not follow a rigid classification, and multiple pathways may contribute to these processes with respect to the changes in the saturation level, Ca^{2+} and urea concentrations, availability of the organic materials, and the nature of EPS at the timescale of the experiment. Our results can also be used to constrain a set of experimental conditions for synthesizing a certain polymorph ratio for vaterite/calcite or a particular morphology of each polymorph.

4. MATERIAL AND METHODS

4.1. Material and Sample Preparation. *S. pasteurii* (ATCC 11859) was obtained from the American Type Culture Collection (ATCC). Bacteria were inoculated into a sterile liquid growth medium and grown in a 30 °C shaker incubator (150 rpm) for 48 h. The composition of the liquid growth medium was nutrient broth (3 g/L), urea (10 g/L), NH_4Cl (10 g/L), and $NaHCO_3$ (2.12 g/L). Meanwhile, the agar-based growth medium was prepared with the same ingredients with the addition of 15 g/L agar. After growth in the liquid growth medium for 48 h, the bacterial cell concentration was determined by serial dilution and plating on the agar growth medium and correlated with the optical density of the liquid culture at a wavelength of 600 nm (OD_{600}) using a UV−vis spectrophotometer. Bacteria were maintained on agar-based growth medium plates at 21 °C for further investigations. Every few weeks, fresh agar plate cultures were prepared from frozen stocks of the original culture.

4.2. Experimental Procedure. *4.2.1. Effects of Calcium and Urea Concentrations.* Different concentrations of $CaCl_2$ as a calcium source and urea required for ureolytic activity and production of carbonate ions (CO_3^{2-}) were added to 1000 mL flasks of deionized water. The concentrations of Ca^{2+} and urea

https://doi.org/10.1021/acsomega.1c00559
ACS Omega 2021, 6, 11988−12003

used in the experiments are summarized in Table 1 (samples 1−8), where the molar ratio of Ca^{2+} and urea was kept at 1. The pH values of the solutions (biomineralization solution) were measured to be around 5.5 to 6. The pH of each solution was then raised to 9.00 by the addition of solid NaOH to achieve the optimum pH value for the *S. pasteurii* ureolytic activity. Concentrated bacterial cultures were diluted to 10^7 cell/mL and added to the biomineralization solution. The biomineralization solutions were then stored in 1000 mL Erlenmeyer flasks in a walk-in environmental chamber at 30 °C on a shaker at a speed of 150 rpm. The flask opening was covered loosely with a foil to maintain sterility, prevent evaporation, and to allow oxygen flow into the solution. After 24 h, the biomineralization solutions were filtrated using a Metricel GA-6 filter membrane with a 47 mm diameter and a 0.45 μm pore size and $CaCO_3$ precipitates were collected. For each sample, the precipitate was divided into two sections. One section was gently rinsed with deionized water to remove bacterial cells and excess organic molecules that were not incorporated into the crystal structures. These samples were then ground into a powder and used for phase identification by powder XRD, FTIR, EDS, and TGA techniques. The other section was utilized to observe the morphology of precipitated particles and the bacterial cell's participation in the precipitation process by SEM. For SEM analysis, precipitates were dried at 40 °C under vacuum for 12 h. The drying temperature was kept relatively low in order to prevent probable transformation of $CaCO_3$ polymorphs.

4.2.2. Time-Dependent Biomineralization Kinetics. The same preparation path was also followed to study the time-dependent biomineralization kinetics. The experiment was carried out by preparing a continuously stirred 1000 mL flask of biomineralization solution (concentrations of Ca^{2+} and urea were set at 0.5 M). Continuous measurements of pH and EC of the biomineralization solution were performed using a Hanna HI5522-01 pH/ISE/EC meter. The pH and EC readings were captured every 30 s for 30 days in the walk-in environmental chamber at 30 °C. Measurements were interrupted several times during the test whenever precipitated calcium carbonate accumulated in the electrodes. The electrodes were cleaned by dissolving the precipitates in 1 M HCl and rinsing with deionized water. The precipitates were removed at various time intervals (samples 9−15 in Table 1) to study the compositional and morphological evolution of $CaCO_3$ particles when a dramatic change was observed in the pH or/and EC profile.

4.3. Characterization. Phase identification of powder samples was assessed by XRD. The XRD patterns were collected by scanning between 5° and 80° (2θ) in the continuous mode by employing a Philips X'pert diffractometer in the θ−θ configuration using Cu Kα (k = 1.54 Å) radiation. The diffractometer was run in the continuous mode with an integrated step scan of 0.021° (2θ) using a PiXcel detector with a time per step of 150 s. To quantitatively examine the polymorph content of $CaCO_3$ precipitates, the powder XRD patterns were analyzed using the Rietveld refinement method with the material analysis using diffraction package.[3,94]

Organic compounds associated with $CaCO_3$ polymorphs were quantified using a TGA (STA 6000, PerkinElmer). Around 30 mg of each powder was placed in pure aluminum oxide crucibles and heated at a rate of 15 °C/min over a temperature range of 35−1000 °C under a UHP-N_2 gas purged at a flow rate of 20 mL/min. The mass loss (TG) and the differential mass loss (DTG) traces were used to calculate the residual organic compounds present in the systems.[95]

FTIR and EDS analyses were performed to further identify the incorporated organic compounds in the structure of $CaCO_3$ polymorphs. FTIR spectra were recorded using a Nicolet Impact 400 FTIR spectrometer from 4000 to 400 cm^{-1} at room temperature and EDS elemental mapping was performed along with SEM on the surface of the $CaCO_3$ polymorphs. Polymorph selection and morphological evolution of $CaCO_3$ precipitates were observed by SEM imaging. Every SEM sample was mounted on a specimen holder by the means of double-sided carbon adhesives. Loose particles were removed by a hand blower, and samples were gold-coated before being placed into the SEM chamber.

AUTHOR INFORMATION

Corresponding Author

Hongyan Ma − *Department of Civil, Architectural and Environmental Engineering, Missouri University of Science and Technology, Rolla, Missouri 65401, United States;* orcid.org/0000-0003-3674-3845; Phone: (573) 612-9568; Email: mahon@mst.edu

Authors

Maryam Khanjani − *Department of Civil, Architectural and Environmental Engineering, Missouri University of Science and Technology, Rolla, Missouri 65401, United States*

David J. Westenberg − *Department of Biological Sciences, Missouri University of Science and Technology, Rolla, Missouri 65401, United States*

Aditya Kumar − *Department of Materials Science and Engineering, Missouri University of Science and Technology, Rolla, Missouri 65401, United States;* orcid.org/0000-0001-7550-8034

Complete contact information is available at: https://pubs.acs.org/10.1021/acsomega.1c00559

Notes

The authors declare no competing financial interest.

ACKNOWLEDGMENTS

We sincerely thank Wenyu Liao from the Missouri University of Science and Technology (S&T) for acquiring the FTIR data. We also thank the technical support provided by the Advanced Materials Characterization Laboratory and Materials Research Center at Missouri S&T. Financial support from the National Science Foundation (under CMMI-1761697) is gratefully acknowledged. Any opinions, findings, and conclusions or recommendations expressed in this material are those of the authors and do not reflect the views of the National Science Foundation.

REFERENCES

(1) Chunxiang, Q.; Jianyun, W.; Ruixing, W.; Liang, C. Corrosion Protection of Cement-Based Building Materials by Surface Deposition of $CaCO_3$ by *Bacillus pasteurii*. *Mater. Sci. Eng., C* **2009**, *29*, 1273−1280.

(2) Costa, L. M. M.; Olyveira, G. M.; Salomão, R. Precipitated Calcium Carbonate Nano-Microparticles: Applications in Drug Delivery. *Adv. Tissue Eng. Regen. Med. Open Access* **2017**, 3, No. 00059.

(3) Lutterotti, L.; Matthies, S.; Wenk, H.-R.; Schultz, A. S.; Richardson, J. W., Jr. Combined Texture and Structure Analysis of

Deformed Limestone from Time-of-Flight Neutron Diffraction Spectra. *J. Appl. Phys.* **1997**, *81*, 594−600.
(4) Meldrum, F. C. Calcium Carbonate in Biomineralisation and Biomimetic Chemistry. *Int. Mater. Rev.* **2003**, *48*, 187−224.
(5) Zou, Z.; Habraken, W. J.; Matveeva, G.; Jensen, A. C.; Bertinetti, L.; Hood, M. A.; Sun, C.; Gilbert, P. U.; Polishchuk, I.; Pokroy, B. A Hydrated Crystalline Calcium Carbonate Phase: Calcium Carbonate Hemihydrate. *Science* **2019**, *363*, 396−400.
(6) Kulak, A. N.; Iddon, P.; Li, Y.; Armes, S. P.; Cölfen, H.; Paris, O.; Wilson, R. M.; Meldrum, F. C. Continuous Structural Evolution of Calcium Carbonate Particles: A Unifying Model of Copolymer-Mediated Crystallization. *J. Am. Chem. Soc.* **2007**, *129*, 3729−3736.
(7) Rodriguez-Navarro, C.; Jimenez-Lopez, C.; Rodriguez-Navarro, A.; Gonzalez-Munoz, M. T.; Rodriguez-Gallego, M. Bacterially Mediated Mineralization of Vaterite. *Geochim. Cosmochim. Acta* **2007**, *71*, 1197−1213.
(8) Wu, J.; Zeng, R. J. Biomimetic Regulation of Microbially Induced Calcium Carbonate Precipitation Involving Immobilization of Sporasarcina Pasteurii by Sodium Alginate. *Cryst. Growth Des.* **2017**, *17*, 1854−1862.
(9) Sand, K. K.; Rodriguez-Blanco, J. D.; Makovicky, E.; Benning, L. G.; Stipp, S. L. S. Crystallization of $CaCO_3$ in Water−Alcohol Mixtures: Spherulitic Growth, Polymorph Stabilization, and Morphology Change. *Cryst. Growth Des.* **2012**, *12*, 842−853.
(10) Wang, Y.-Y.; Yao, Q.-Z.; Li, H.; Zhou, G.-T.; Sheng, Y.-M. Formation of Vaterite Mesocrystals in Biomineral-like Structures and Implication for Biomineralization. *Cryst. Growth Des.* **2015**, *15*, 1714−1725.
(11) Svenskaya, Y. I.; Fattah, H.; Inozemtseva, O. A.; Ivanova, A. G.; Shtykov, S. N.; Gorin, D. A.; Parakhonskiy, B. V. Key Parameters for Size-and Shape-Controlled Synthesis of Vaterite Particles. *Cryst. Growth Des.* **2018**, *18*, 331−337.
(12) Torres-Aravena, Á. E.; Duarte-Nass, C.; Azócar, L.; Mella-Herrera, R.; Rivas, M.; Jeison, D. Can Microbially Induced Calcite Precipitation (MICP) through a Ureolytic Pathway Be Successfully Applied for Removing Heavy Metals from Wastewaters? *Crystals* **2018**, *8*, No. 438.
(13) Kawaguchi, T.; Decho, A. W. A Laboratory Investigation of Cyanobacterial Extracellular Polymeric Secretions (EPS) in Influencing $CaCO_3$ Polymorphism. *J. Cryst. Growth* **2002**, *240*, 230−235.
(14) Bianconi, P. A.; Lin, J.; Strzelecki, A. R. Crystallization of an Inorganic Phase Controlled by a Polymer Matrix. *Nature* **1991**, *349*, 315−317.
(15) Wang, L.; Sondi, I.; Matijević, E. Preparation of Uniform Needle-like Aragonite Particles by Homogeneous Precipitation. *J. Colloid Interface Sci.* **1999**, *218*, 545−553.
(16) Ghosh, T.; Bhaduri, S.; Montemagno, C.; Kumar, A. Sporosarcina Pasteurii Can Form Nanoscale Calcium Carbonate Crystals on Cell Surface. *PLoS One* **2019**, *14*, No. e0210339.
(17) Sondi, I.; Matijević, E. Homogeneous Precipitation of Calcium Carbonates by Enzyme Catalyzed Reaction. *J. Colloid Interface Sci.* **2001**, *238*, 208−214.
(18) Chen, L.; Shen, Y.; Xie, A.; Huang, B.; Jia, R.; Guo, R.; Tang, W. Bacteria-Mediated Synthesis of Metal Carbonate Minerals with Unusual Morphologies and Structures. *Cryst. Growth Des.* **2009**, *9*, 743−754.
(19) Luo, M.; Qian, C.; Li, R. Factors Affecting Crack Repairing Capacity of Bacteria-Based Self-Healing Concrete. *Constr. Build. Mater.* **2015**, *87*, 1−7.
(20) Hammes, F.; Boon, N.; de Villiers, J.; Verstraete, W.; Siciliano, S. D. Strain-Specific Ureolytic Microbial Calcium Carbonate Precipitation. *Appl. Environ. Microbiol.* **2003**, *69*, 4901−4909.
(21) Dhami, N. K.; Reddy, M. S.; Mukherjee, A. Bacillus Megaterium Mediated Mineralization of Calcium Carbonate as Biogenic Surface Treatment of Green Building Materials. *World J. Microbiol. Biotechnol.* **2013**, *29*, 2397−2406.
(22) Meldrum, F. C.; Cölfen, H. Controlling Mineral Morphologies and Structures in Biological and Synthetic Systems. *Chem. Rev.* **2008**, *108*, 4332−4432.
(23) Chiu, C. H. *Screening of Microorganisms, Calcium Sources, and Protective Materials for Self-Healing Concrete.* PhD Thesis , Purdue University Graduate School, 2019.
(24) Stocks-Fischer, S.; Galinat, J. K.; Bang, S. S. Microbiological Precipitation of $CaCO_3$. *Soil Biol. Biochem.* **1999**, *31*, 1563−1571.
(25) Hammes, F.; Verstraete, W. Key Roles of PH and Calcium Metabolism in Microbial Carbonate Precipitation. *Rev. Environ. Sci. Biotechnol.* **2002**, *1*, 3−7.
(26) Bhaduri, S.; Debnath, N.; Mitra, S.; Liu, Y.; Kumar, A. Microbiologically Induced Calcite Precipitation Mediated by Sporosarcina Pasteurii. *JoVE J. Vis. Exp.* **2016**, *110*, No. e53253.
(27) Phillips, A. J.; Gerlach, R.; Lauchnor, E.; Mitchell, A. C.; Cunningham, A. B.; Spangler, L. Engineered Applications of Ureolytic Biomineralization: A Review. *Biofouling* **2013**, *29*, 715−733.
(28) De Muynck, W.; De Belie, N.; Verstraete, W. Microbial Carbonate Precipitation in Construction Materials: A Review. *Ecol. Eng.* **2010**, *36*, 118−136.
(29) Anbu, P.; Kang, C.-H.; Shin, Y.-J.; So, J.-S. Formations of Calcium Carbonate Minerals by Bacteria and Its Multiple Applications. *Springerplus* **2016**, *5*, 1−26.
(30) Morita, R. Y. Calcite Precipitation by Marine Bacteria. *Geomicrobiol. J.* **1980**, *2*, 63−82.
(31) Ehrlich, H.; Geomicrobiology, L. Its Significance for Geology. *Earth-Sci. Rev.* **1998**, *45*, 45−60.
(32) Ferris, F. G.; Stehmeier, L. G.; Kantzas, A.; Mourits, F. M. Bacteriogenic Mineral Plugging. *J. Can. Pet. Technol.* **1997**, *36* (), DOI: 10.2118/97-09-07.
(33) Ghashghaei, S.; Emtiazi, G. Production of Calcite Nanocrystal by a Urease-Positive Strain of Enterobacter Ludwigii and Study of Its Structure by SEM. *Curr. Microbiol.* **2013**, *67*, 406−413.
(34) Douglas, S.; Beveridge, T. J. Mineral Formation by Bacteria in Natural Microbial Communities. *FEMS Microbiol. Ecol.* **1998**, *26*, 79−88.
(35) Arias, J. L.; Fernández, M. S. Polysaccharides and Proteoglycans in Calcium Carbonate-Based Biomineralization. *Chem. Rev.* **2008**, *108*, 4475−4482.
(36) Bang, S. S.; Galinat, J. K.; Ramakrishnan, V. Calcite Precipitation Induced by Polyurethane-Immobilized Bacillus Pasteurii. *Enzyme Microb. Technol.* **2001**, *28*, 404−409.
(37) Mitchell, A. C.; Ferris, F. G. The Influence of Bacillus Pasteurii on the Nucleation and Growth of Calcium Carbonate. *Geomicrobiol. J.* **2006**, *23*, 213−226.
(38) Achal, V.; Mukherjee, A.; Basu, P. C.; Reddy, M. S. Strain Improvement of Sporosarcina Pasteurii for Enhanced Urease and Calcite Production. *J. Ind. Microbiol. Biotechnol.* **2009**, *36*, 981−988.
(39) Okwadha, G. D.; Li, J. Optimum Conditions for Microbial Carbonate Precipitation. *Chemosphere* **2010**, *81*, 1143−1148.
(40) Reddy, M. S. Biomineralization of Calcium Carbonates and Their Engineered Applications: A Review. *Front. Microbiol.* **2013**, *4*, 314.
(41) Gibbs, J. W. On the Equilibrium of Heterogeneous Substances. *Am. J. Sci.* **1878**, *96*, 441−458.
(42) Lecomte, C. Polymorphism in Molecular Crystals. By Joel Bernstein. Oxford University Press, 2020, pp. 608, Hardcover. Price GBP 85.00. ISBN 9780199655441. *Acta Crystallogr., Sect. B: Struct. Sci., Cryst. Eng. Mater.* **2021**, *77*, 184−185.
(43) Cardew, P. T.; Davey, R. J. The Kinetics of Solvent-Mediated Phase Transformations. *Proc. R. Soc. Lond. A. Math. Phys. Sci.* **1815**, *1985*, 415−428.
(44) Gebauer, D.; Cölfen, H. Prenucleation Clusters and Non-Classical Nucleation. *Nano Today* **2011**, *6*, 564−584.
(45) Gebauer, D.; Gunawidjaja, P. N.; Ko, J. P.; Bacsik, Z.; Aziz, B.; Liu, L.; Hu, Y.; Bergström, L.; Tai, C.-W.; Sham, T.-K. Proto-Calcite and Proto-Vaterite in Amorphous Calcium Carbonates. *Angew. Chem., Int. Ed.* **2010**, *49*, 8889−8891.
(46) Gebauer, D.; Völkel, A.; Cölfen, H. Stable Prenucleation Calcium Carbonate Clusters. *Science* **2008**, *322*, 1819−1822.

https://doi.org/10.1021/acsomega.1c00559
ACS Omega 2021, 6, 11988−12003

(47) Cöelfen, H.; Antonietti, M. *Mesocrystals and Nonclassical Crystallization*; John Wiley & Sons, 2008, DOI: 10.1002/9780470994603.
(48) Bots, P.; Benning, L. G.; Rodriguez-Blanco, J.-D.; Roncal-Herrero, T.; Shaw, S. Mechanistic Insights into the Crystallization of Amorphous Calcium Carbonate (ACC). *Cryst. Growth Des.* **2012**, *12*, 3806−3814.
(49) Pouget, E. M.; Bomans, P. H.; Goos, J. A.; Frederik, P. M.; Sommerdijk, N. A. The Initial Stages of Template-Controlled CaCO3 Formation Revealed by Cryo-TEM. *Science* **2009**, *323*, 1455−1458.
(50) Du, H.; Amstad, E. Water: How Does It Influence the CaCO3 Formation? *Angew. Chem., Int. Ed.* **2020**, *59*, 1798−1816.
(51) Mann, S. *Biomineralization: Principles and Concepts in Bioinorganic Materials Chemistry*. Oxford University Press 2001, *5*.
(52) De Yoreo, J. J.; Vekilov, P. G. Principles of Crystal Nucleation and Growth. *Rev. Mineral. Geochem.* **2003**, *54*, 57−93.
(53) Mann, S. Molecular Tectonics in Biomineralization and Biomimetic Materials Chemistry. *Nature* **1993**, *365*, 499−505.
(54) Braissant, O.; Cailleau, G.; Dupraz, C.; Verrecchia, E. P. Bacterially Induced Mineralization of Calcium Carbonate in Terrestrial Environments: The Role of Exopolysaccharides and Amino Acids. *J. Sediment. Res.* **2003**, *73*, 485−490.
(55) Zhou, G.-T.; Yao, Q.-Z.; Fu, S.-Q.; Guan, Y.-B. Controlled Crystallization of Unstable Vaterite with Distinct Morphologies and Their Polymorphic Transition to Stable Calcite. *Eur. J. Mineral.* **2010**, *22*, 259−269.
(56) Repo, E.; Warchoł, J. K.; Bhatnagar, A.; Sillanpää, M. Heavy Metals Adsorption by Novel EDTA-Modified Chitosan−Silica Hybrid Materials. *J. Colloid Interface Sci.* **2011**, *358*, 261−267.
(57) Chakrabarty, D.; Mahapatra, S. Aragonite Crystals with Unconventional Morphologies. *J. Mater. Chem.* **1999**, *9*, 2953−2957.
(58) Xyla, A. G.; Koutsoukos, P. G. Quantitative Analysis of Calcium Carbonate Polymorphs by Infrared Spectroscopy. *J. Chem. Soc., Faraday Trans. 1* **1989**, *85*, 3165−3172.
(59) Vagenas, N. V.; Gatsouli, A.; Kontoyannis, C. G. Quantitative Analysis of Synthetic Calcium Carbonate Polymorphs Using FT-IR Spectroscopy. *Talanta* **2003**, *59*, 831−836.
(60) Loste, E.; Wilson, R. M.; Seshadri, R.; Meldrum, F. C. The Role of Magnesium in Stabilising Amorphous Calcium Carbonate and Controlling Calcite Morphologies. *J. Cryst. Growth* **2003**, *254*, 206−218.
(61) Tas, A. C. Monodisperse Calcium Carbonate Microtablets Forming at 70° C in Prerefrigerated CaCl2−Gelatin−Urea Solutions. *Int. J. Appl. Ceram. Technol.* **2009**, *6*, 53−59.
(62) Farmer, V. C. *Infrared Spectra of Minerals*; Mineralogical Society, 1974.
(63) Zhou, G.-T.; Jimmy, C. Y.; Wang, X.-C.; Zhang, L.-Z. Sonochemical Synthesis of Aragonite-Type Calcium Carbonate with Different Morphologies. *New J. Chem.* **2004**, *28*, 1027−1031.
(64) Levi, Y.; Albeck, S.; Brack, A.; Weiner, S.; Addadi, L. Control over Aragonite Crystal Nucleation and Growth: An in Vitro Study of Biomineralization. *Chem. − Eur. J.* **1998**, *4*, 389−396.
(65) Gabrielli, C.; Jaouhari, R.; Joiret, S.; Maurin, G. In Situ Raman Spectroscopy Applied to Electrochemical Scaling. Determination of the Structure of Vaterite. *J. Raman Spectrosc.* **2000**, *31*, 497−501.
(66) Mason, T. J. *Sonochemistry*; Royal Society of Chemistry Cambridge, U. K., 1990.
(67) Rautaray, D.; Ahmad, A.; Sastry, M. Biosynthesis of $CaCO_3$ Crystals of Complex Morphology Using a Fungus and an Actinomycete. *J. Am. Chem. Soc.* **2003**, *125*, 14656−14657.
(68) Fleming, I.; Williams, D. H. *Spectroscopic Methods in Organic Chemistry*; McGraw-Hill New York, 1966.
(69) Pryce, R. S.; Hench, L. L. Tailoring of Bioactive Glasses for the Release of Nitric Oxide as an Osteogenic Stimulus. *J. Mater. Chem.* **2004**, *14*, 2303−2310.
(70) Muresan, D.; Bularda, M. D.; Popa, C.; Baia, L.; Simon, S. Structural and Biological Investigations of Phosphate Glasses with Silver. *Rom. J. Phys.* **2006**, *51*, 231.
(71) Decho, A. W. Microbial Biofilms in Intertidal Systems: An Overview. *Cont. Shelf Res.* **2000**, *20*, 1257−1273.
(72) Beveridge, T. J.; Graham, L. L. Surface Layers of Bacteria. *Microbiol. Mol. Biol. Rev.* **1991**, *55*, 684−705.
(73) Wingender, J.; Neu, T. R.; Flemming, H.-C. What Are Bacterial Extracellular Polymeric Substances? In *Microbial extracellular polymeric substances*; Springer, 1999; pp. 1−19.
(74) McSwain, B. S.; Irvine, R. L.; Hausner, M.; Wilderer, P. A. Composition and Distribution of Extracellular Polymeric Substances in Aerobic Flocs and Granular Sludge. *Appl. Environ. Microbiol.* **2005**, *71*, 1051−1057.
(75) Li, Y.; Sun, H.; Ma, X.; Lu, A.; Lux, R.; Zusman, D.; Shi, W. Extracellular Polysaccharides Mediate Pilus Retraction during Social Motility of Myxococcus Xanthus. *Proc. Natl. Acad. Sci. U. S. A.* **2003**, *100*, 5443−5448.
(76) Falini, G.; Fermani, S.; Gazzano, M.; Ripamonti, A. Polymorphism and Architectural Crystal Assembly of Calcium Carbonate in Biologically Inspired Polymeric Matrices. *J. Chem. Soc., Dalton Trans.* **2000**, *21*, 3983−3987.
(77) Thiery, M.; Villain, G.; Dangla, P.; Platret, G. Investigation of the Carbonation Front Shape on Cementitious Materials: Effects of the Chemical Kinetics. *Cem. Concr. Res.* **2007**, *37*, 1047−1058.
(78) Pallagi, A.; Tasi, Á.; Gácsi, A.; Csáti, M.; Pálinkó, I.; Peintler, G.; Sipos, P. The Solubility of $Ca(OH)_2$ in Extremely Concentrated NaOH Solutions at 25 C. *Cent. Eur. J. Chem.* **2012**, *10*, 332−337.
(79) Smith, R. M.; Martell, A. E. *Critical Stability Constants: Inorganic Complexes*. Springer 1976, *4*.
(80) Johnston, J. The Several Forms of Calcium Carbonate. *Am. J. Sci.* **1916**, 473−512.
(81) Brečević, L.; Nielsen, A. E. Solubility of Amorphous Calcium Carbonate. *J. Cryst. Growth* **1989**, *98*, 504−510.
(82) Radha, A. V.; Forbes, T. Z.; Killian, C. E.; Gilbert, P.; Navrotsky, A. Transformation and Crystallization Energetics of Synthetic and Biogenic Amorphous Calcium Carbonate. *Proc. Natl. Acad. Sci. U. S. A.* **2010**, *107*, 16438−16443.
(83) Nielsen, M. H.; Lee, J. R.; Hu, Q.; Han, T. Y.-J.; De Yoreo, J. J. Structural Evolution, Formation Pathways and Energetic Controls during Template-Directed Nucleation of $CaCO_3$. *Faraday Discuss.* **2012**, *159*, 105−121.
(84) Leveling, T. The Relationship between PH and Conductivity in a Lithium Contaminated. *De-Ionized Water System; FNAL Pbar Note* 2002, *674*.
(85) Ren, D.; Feng, Q.; Bourrat, X. The Co-Effect of Organic Matrix from Carp Otolith and Microenvironment on Calcium Carbonate Mineralization. *Mater. Sci. Eng., C* **2013**, *33*, 3440−3449.
(86) Hu, Q.; Nielsen, M. H.; Freeman, C. L.; Hamm, L. M.; Tao, J.; Lee, J. R. I.; Han, T. Y.-J.; Becker, U.; Harding, J. H.; Dove, P. M. The Thermodynamics of Calcite Nucleation at Organic Interfaces: Classical vs. Non-Classical Pathways. *Faraday Discuss.* **2012**, *159*, 509−523.
(87) Ruiz-Agudo, E.; Di Tommaso, D.; Putnis, C. V.; de Leeuw, N. H.; Putnis, A. Interactions between Organophosphonate-Bearing Solutions and (1014) Calcite Surfaces: An Atomic Force Microscopy and First-Principles Molecular Dynamics Study. *Cryst. Growth Des.* **2010**, *10*, 3022−3035.
(88) Wang, T.; Antonietti, M.; Cölfen, H. Calcite Mesocrystals:"-Morphing" Crystals by a Polyelectrolyte. *Chem. − Eur. J.* **2006**, *12*, 5722−5730.
(89) Travaille, A. M.; Donners, J. J.; Gerritsen, J. W.; Sommerdijk, N. A.; Nolte, R. J.; van Kempen, H. Aligned Growth of Calcite Crystals on a Self-Assembled Monolayer. *Adv. Mater.* **2002**, *14*, 492−495.
(90) Han, Y.-J.; Aizenberg, J. Face-Selective Nucleation of Calcite on Self-Assembled Monolayers of Alkanethiols: Effect of the Parity of the Alkyl Chain. *Angew. Chem., Int. Ed.* **2003**, *42*, 3668−3670.
(91) Mao, Z.; Huang, J. Habit Modification of Calcium Carbonate in the Presence of Malic Acid. *J. Solid State Chem.* **2007**, *180*, 453−460.

https://doi.org/10.1021/acsomega.1c00559
ACS Omega 2021, 6, 11988−12003

(92) López-Macipe, A.; Gómez-Morales, J.; Rodríguez-Clemente, R. The Role of PH in the Adsorption of Citrate Ions on Hydroxyapatite. *J. Colloid Interface Sci.* **1998**, *200*, 114−120.
(93) Wada, N.; Yamashita, K.; Umegaki, T. Effects of Carboxylic Acids on Calcite Formation in the Presence of Mg2+ Ions. *J. Colloid Interface Sci.* **1999**, *212*, 357−364.
(94) Dickinson, S. R.; McGrath, K. M. Quantitative Determination of Binary and Tertiary Calcium Carbonate Mixtures Using Powder X-Ray Diffraction. *Analyst* **2001**, *126*, 1118−1121.
(95) Stoian, J.; Oey, T.; Bullard, J. W.; Huang, J.; Kumar, A.; Balonis, M.; Terrill, J.; Neithalath, N.; Sant, G. New Insights into the Prehydration of Cement and Its Mitigation. *Cem. Concr. Res.* **2015**, *70*, 94−103.

https://doi.org/10.1021/acsomega.1c00559
ACS Omega 2021, 6, 11988−12003